

Manipulation of ferromagnetic damping via antiferromagnetic Néel order based on spin-pumping theory

Ze Li(李泽), Yi Liu(刘翌), Zhe Yuan(袁喆)

Citation: Chin. Phys. B. 35, 097202 (2026). DOI: 10.1088/1674-1056/ae6d9c |
CSTR: 32038.14.CPB.ae6d9c
http://cpb.iphy.ac.cn; http://iopscience.iop.org/cpb

What follows is a list of articles you may be interested in

In-phase and out-of-phase spin pumping effects in Py/Ru/Py synthetic antiferromagnetic structures

Zhaocong Huang(黄兆聪), Xuejian Tang(唐学健), Qian Chen(陈倩), Wei Jiang(蒋伟), Qingjie Guo(郭庆杰), Milad Jalali, Jun Du(杜军), Ya Zhai(翟亚)
Chin. Phys. B. 33, 097202 (2024). DOI: 10.1088/1674-1056/ad553d

Spin transport characteristics modulated by the GeBi interlayer in $Y_3Fe_5O_{12}$/GeBi/Pt heterostructures

Mingming Li(李明明), Lei Zhang(张磊), Lichuan Jin(金立川), Haizhong Guo(郭海中)
Chin. Phys. B. 33, 027201 (2024). DOI: 10.1088/1674-1056/ace3aa

Inverse spin Hall effect in ITO/YIG exited by spin pumping and spin Seebeck experiments

Kejian Zhu(朱科建), Weijian Lin(林伟坚), Yangtao Su(苏仰涛), Haibin Shi(石海滨), Yang Meng(孟洋), Hongwu Zhao(赵宏武)
Chin. Phys. B. 28, 017201 (2019). DOI: 10.1088/1674-1056/28/1/017201

The origin of spin current in YIG/nonmagnetic metal multilayers at ferromagnetic resonance

Yun Kang(康韵), Hai Zhong(钟海), Runrun Hao(郝润润), Shujun Hu(胡树军), Shishou Kang(康仕寿), Guolei Liu(刘国磊), Yin Zhang(张引), Xiangrong Wang(王向荣), Shishen Yan(颜世申), Yong Wu(吴勇), Shuyun Yu(于淑云), Guangbing Han(韩广兵), Yong Jiang(姜勇), Liangmo Mei(梅良模)
Chin. Phys. B. 26, 047202 (2017). DOI: 10.1088/1674-1056/26/4/047202

Adiabatic quantum pump in a zigzag graphene nanoribbon junction

Zhang Lin(张林)
Chin. Phys. B. 24, 117202 (2015). DOI: 10.1088/1674-1056/24/11/117202

RAPID COMMUNICATION

Manipulation of ferromagnetic damping via antiferromagnetic Néel order based on spin-pumping theory

Ze Li(李泽)[1], Yi Liu(刘翌)[2,3,†], and Zhe Yuan(袁喆)[1,‡]

[1] *State Key Laboratory of Surface Physics, and Interdisciplinary Center for Theoretical Physics and Information Sciences, Fudan University, Shanghai* 200433, *China*

[2] *Institute for Quantum Science and Technology, Shanghai University, Shanghai* 200444, *China*

[3] *Department of Physics, Shanghai University, Shanghai* 200444, *China*

(Received 1 April 2026; revised manuscript received 12 May 2026; accepted manuscript online 14 May 2026)

Magnetic damping in ferromagnets is a central parameter in spin dynamics and device design. Here, we combine spin-pumping theory with the first-principles scattering-matrix method to investigate how an $L1_0$-MnPd antiferromagnetic layer modifies the damping of an adjacent $Ni_{80}Fe_{20}$ alloy (Py) layer. In the heterostructure Cu|MnPd|Py|MnPd|Cu, we analyze the angular dependence of the damping enhancement for five representative magnetic configurations. When the pumped spin-current polarization is perpendicular to the Néel vector, the antiferromagnet acts as an efficient spin sink and strongly enhances the damping. When the spin current is polarized parallel to the Néel vector, spin backflow suppresses the net spin-current injection and markedly reduces the damping enhancement. The angular dependence shows a dominant twofold symmetry with a weaker fourfold component. This behavior can be quantitatively explained by the vector structure of the spin-transfer torque. Additional tests involving Cu-spacer insertion, MnPd thickness variation, and several forms of disorder — including spin disorder, lattice disorder, and interface disorder — confirm the robustness of this mechanism. These results identify the Néel order as a new degree of freedom for tuning ferromagnetic damping and provide a theoretical basis for designing antiferromagnet-based spintronic devices with controllable damping.

Keywords: spin pumping, magnetic damping, FM|AFM, MnPd

PACS: 72.25.Mk, 75.76.+j, 75.50.Ee

DOI: 10.1088/1674-1056/ae6d9c **CSTR:** 32038.14.CPB.ae6d9c

1. Introduction

The magnetic damping of a ferromagnet (FM) characterizes the energy dissipation during magnetization precession. It is a key factor that governs spin dynamics and limits the operating frequency of magnetic devices. In thin-film and multilayer structures, adjacent layers and interfaces can substantially modify the damping of an FM, making interfacial damping engineering a central issue in ultrathin magnetic heterostructures.[1–3] From a physical perspective, the damping is often separated into intrinsic and nonlocal contributions. The intrinsic part is governed mainly by spin–orbit coupling and electronic scattering inside the FM itself, and its material dependence in Fe, Co, and Ni has been systematically studied experimentally[4–7] and from first principles.[8,9] The nonlocal part originates from interfacial spin–angular-momentum exchange and is naturally described by spin pumping[10,11] and by the scattering theory of Gilbert damping.[12] In the spin-pumping mechanism, a precessing FM at ferromagnetic resonance ejects a pure spin current into adjacent layers, thereby enhancing the effective Gilbert damping of the FM. This process is determined by both the spin-mixing conductance and spin backflow.[2,3,10] Recent studies further show that magnetic damping and spin pumping can be strongly affected by dynamic magnetic configurations.[13] This highlights that spin-current relaxation is sensitive not only to the interface but also to the relative dynamics of magnetic layers.

In conventional FM/heavy-metal bilayers, the strong spin–orbit coupling of the adjacent heavy-metal layer makes it an efficient spin sink. This enhances the spin-pumping-induced damping and also enables conversion of the spin current into a detectable charge signal through the inverse spin Hall effect.[14,15] In this framework, interfacial spin transport and damping modulation have become important experimental tools in spin–orbit electronics. They provide a standard route for quantifying the interfacial spin-mixing conductance and spin diffusion.[2,3,14,15]

In recent years, antiferromagnetic spintronics has extended the role of antiferromagnets (AFMs) from conventional static pinning layers to active functional layers that can participate in spin generation, transport, and absorption.[16–20] In FM/AFM heterostructures, the AFM not only influences the static magnetic properties of the FM through exchange bias[21] but also serves as a spin sink that mediates angular-momentum

†Corresponding author. E-mail: yiliu42@shu.edu.cn

‡Corresponding author. E-mail: yuanz@fudan.edu.cn

© 2026 Chinese Physical Society and IOP Publishing Ltd. All rights, including for text and data mining, AI training, and similar technologies, are reserved.

dissipation during magnetization dynamics.[22,23] Recent experiments further show that this dissipation depends on both the symmetry and the direction of the antiferromagnetic order. Wang *et al*. observed a fourfold symmetric damping anisotropy in exchange-biased CoFeB/$IrMn_3$ bilayers, where $IrMn_3$ has a noncollinear antiferromagnetic order, and attributed it to uncompensated antiferromagnetic moments.[24] Moriyama *et al*. in exchange-biased Pt/FeMn/FeNi polycrystalline films[25] and Polishchuk *et al*. in NiFe/Cu/FeMn polycrystalline spin valves[26] both found that the ferromagnetic damping enhancement depends on the angle between the pumped spin-current polarization and the Néel vector. In the former case, the exchange-spring effect prevents the Néel vector from rotating smoothly with the applied field. As a result, only abrupt damping changes within specific angular intervals were observed. In the latter case, the angular dependence is more continuous, but the phenomenological spin-conductance model does not explain its microscopic origin. In contrast, Yang *et al*. found that in the Py/CoO/Ag/Fe system, once the interlayer magnetic coupling is eliminated, the Fe-layer damping becomes insensitive to the Néel-vector orientation of the insulating AFM CoO.[27] These studies indicate that metallic and insulating AFMs exhibit markedly different damping responses to the Néel-vector orientation. They also show that current explanations remain phenomenological or are constrained by experimental conditions. This raises a central question: does spin-current absorption in metallic AFMs intrinsically depend on the Néel-vector orientation, and if so, what is its microscopic origin?

In this work, we choose $L1_0$-MnPd as the AFM layer because of its simple collinear magnetic order and high Néel temperature,[28,29] and the $Ni_{80}Fe_{20}$ alloy (Py) as the FM layer. We combine spin-pumping theory[30] with the first-principles scattering-matrix method[31] and study the symmetric heterostructure Cu|MnPd|Py|MnPd|Cu. This model system has a well-defined magnetic structure and a clear physical picture, which allows us to systematically investigate how the orientation of the Néel order modulates ferromagnetic damping. Compared with the polycrystalline samples, noncollinear magnetic orders, and complex interfacial couplings such as exchange bias and exchange-spring effects encountered in the experiments discussed above, the collinear order of $L1_0$-MnPd allows the Néel-vector direction to be precisely defined and independently controlled. We can therefore examine the intrinsic correlation between the spin current and the Néel order without extraneous complications. By comparing the damping response across different magnetic configurations, we further show that the Néel vector selectively filters the pumped spin current, absorbing the perpendicular component while reflecting the parallel one, thereby giving rise to the angular dependence of the damping. This provides a microscopic explanation for the experimentally observed anisotropy without relying on phenomenological parameters.

2. Electronic structure of MnPd

To validate the adopted $L1_0$-MnPd antiferromagnetic configuration and assess the influence of magnetic-moment orientation on the electronic structure, we calculate the electronic structure of MnPd with different spin-quantization axes, as shown in Fig. 1. The calculations are performed using the DS-PAW first-principles plane-wave method.[32] Figures 1(a), 1(d), and 1(e) show the band dispersion and density of states for quantization axes along [100], [110], and [001], respectively. The three band structures are nearly identical along the full high-symmetry path, with only marginal differences in band crossings and gaps near the Fermi level. This indicates that the band structure is governed mainly by lattice

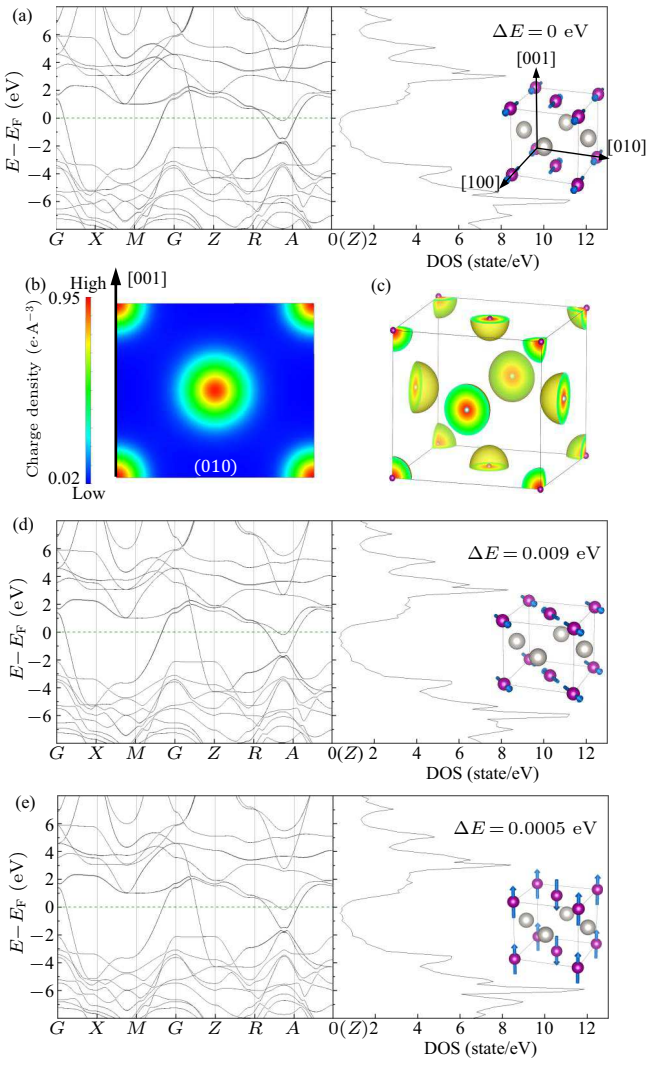


Fig. 1. (a)–(c) Band structure and DOS of MnPd with the Néel-vector orientation along [100], two-dimensional charge-density distribution in the (010) plane (zero offset), with the color scale in units of $e \cdot \text{Å}^{-3}$, and three-dimensional charge-density distribution. (d)–(e) Band structure and DOS of MnPd with the Néel-vector orientation along [110] and [001]. ΔE denotes the total energy difference relative to the [100] Néel-vector configuration.

symmetry. By contrast, the spin–orbit-coupling-induced magnetocrystalline anisotropy has only a minor effect on the band renormalization, so rotating the magnetic-moment direction produces only negligible changes in the electronic structure near the Fermi level. This conclusion is consistent with the damping calculations presented below, which also show little sensitivity to the MnPd Néel-vector orientation. Within a given magnetic structure, rotating the Néel vector changes the total energy only at the 10^{-2} eV level, further confirming the weak magnetic anisotropy of the system. In addition, the lattice constants adopted here, $a^* \approx 2.88$ Å and $c \approx 3.58$ Å, are close to the previous first-principles values $a^* \approx 2.89$ Å and $c \approx 3.60$ Å reported for CuAu-I-type MnPd,[33] which further supports the validity of the structural model used in this work. Figure 1(b) shows the two-dimensional charge-density distribution in the (010) plane, and Fig. 1(c) presents the three-dimensional charge-density distribution. A Bader charge analysis yields average charges of $6.35e$ and $10.65e$ for the Mn and Pd atoms, respectively, with a total net charge of zero, satisfying the charge-neutrality condition. Further calculations confirm that Pd atoms in $L1_0$-MnPd do not carry a stable magnetic moment in the ground state, consistent with neutron-diffraction experiments.[28] A detailed discussion, together with the relevant literature evidence, is given in Appendix A.

3. Damping calculations

Having established the electronic structure of MnPd, we next evaluate the damping enhancement in the symmetric heterostructure Cu|MnPd|Py|MnPd|Cu based on spin-pumping theory and the first-principles scattering-matrix method.[30,31]

3.1. Heterostructure setup

The composite system is shown schematically in Fig. 2(a). The Mn atomic layers serve as contact layers directly adjacent to the Py layer, and the outer MnPd surfaces are connected to semi-infinite Cu electrodes. The atomic matching at the Mn|Py interface is illustrated in Fig. 2(b). The lattice constant of Py is $a_{\mathrm{Py}} = 0.355$ nm, whereas the a-axis lattice constant of MnPd is $a_{\mathrm{MnPd}} = 0.407$ nm. We rotate the Py lattice by 45° and match a supercell of 64 Py atoms per layer to a supercell of 50 MnPd atoms per layer. A small tensile strain is applied to the Py lattice to remove the residual mismatch. Cu is treated in the same way owing to its structural similarity to Py, yielding a total mismatch of 1.32%. We define φ as the angle between the FM magnetization $\boldsymbol{m}$ and the [100] axis. This angle is the central parameter in the subsequent analysis of the angular dependence of the damping. We adopt the symmetric Cu|MnPd|Py|MnPd|Cu geometry to isolate the damping contribution from the MnPd|Py interface. Within this geometry, the two MnPd|Py interfaces are crystallographically and magnetically equivalent, so that their spin-pumping contributions additively contribute to a single intercept. This intercept can therefore be unambiguously attributed to the AFM-induced damping enhancement, leaving the orientation of the MnPd Néel vector as the only remaining variable in the subsequent angular-dependence analysis.

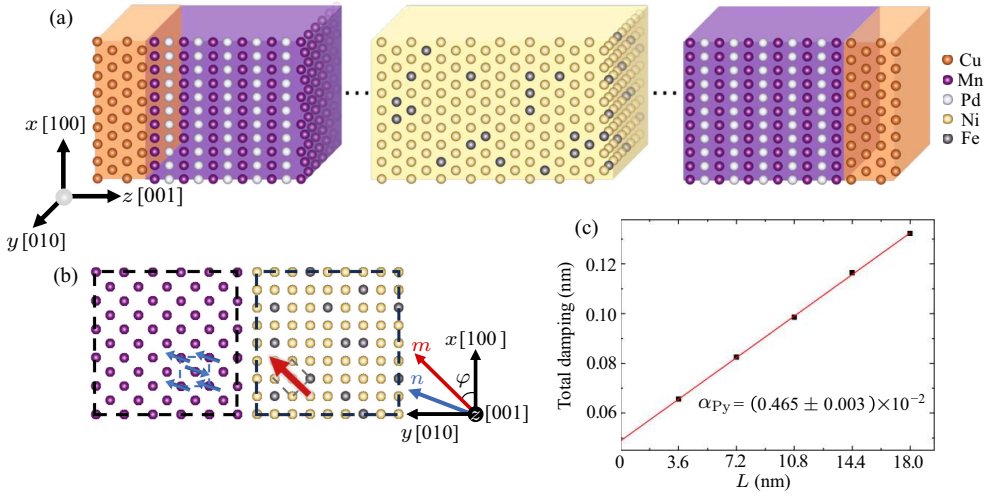


Fig. 2. (a) Schematic of the overall heterostructure. (b) Unit-cell matching of the Cu|MnPd|Py|MnPd|Cu system and the definition of the angle φ. (c) Energy pumping rate as a function of the scattering-region length L for the Cu|Py|Cu system and the corresponding linear fit.

Before constructing the composite system, we calibrate the computational approach using the Cu|Py|Cu system (not shown). The electronic structure is obtained within the tight-binding linear-muffin-tin-orbital method,[34] and the scattering matrix is computed with a first-principles wave-function-matching scheme.[31,35] Following the spin-pumping and scattering-matrix framework of Refs. [30,31], we extract the damping enhancement from the length dependence of the energy pumping rate. As shown in Fig. 2(c), a linear fit to the energy pumping rate of the pure Cu|Py|Cu sys-

tem as a function of the scattering-region length L yields a damping factor $\alpha_{\mathrm{Py}} = (0.465 \pm 0.003) \times 10^{-2}$ and an intercept of $(4.89 \pm 0.02) \times 10^{-2}$ (nm). The slope agrees with the previously reported value $(0.46 \pm 0.02) \times 10^{-2}$ [36] and benchmarks the intrinsic damping of the Py alloy. The intercept represents the interface-related spin-pumping contribution in the reference Cu|Py|Cu system and serves as the baseline for later comparisons. In the subsequent calculations for the Cu|MnPd|Py|MnPd|Cu composite system, we use a constrained linear fit with a fixed slope, namely, a fixed intrinsic damping $\alpha_0 = \alpha_{\mathrm{Py}}$, and extract only the intercept variation. This procedure isolates the intrinsic damping contribution, so any change in the intercept directly reflects the modulation of spin-pumping damping by the Néel order.

3.2. Damping results

To elucidate how the antiferromagnetic order modulates ferromagnetic damping, we consider two limiting cases of coupling between the FM and AFM. In the first, the FM magnetization $\boldsymbol{m}$ and Néel order $\boldsymbol{n} = \boldsymbol{m}_1 - \boldsymbol{m}_2$ (where $\boldsymbol{m}_1$ and $\boldsymbol{m}_2$ are the two sublattice moments) are strongly exchange coupled and their magnetic moments rigidly co-rotate, schematically shown as configurations 1 and 2 in Fig. 3(a), while the corresponding damping results are shown as the gray and orange curves in Fig. 3(b).

For the strong-coupling cases [configurations 1 and 2], the angle φ, measured from the [100] axis, is varied from 0° to 180° in 15° steps within the (001) and (100) planes. Specifically, in configuration 1, $\boldsymbol{m}$ and $\boldsymbol{n}$ are parallel ($\boldsymbol{m} \parallel \boldsymbol{n}$) and co-rotate within the (001) plane. The perturbation $\dot{\boldsymbol{m}}$ is applied along the [001] direction perpendicular to the rotation plane. The pumped spin-current polarization $\boldsymbol{I}_{\mathrm{s}} \propto \boldsymbol{m} \times \dot{\boldsymbol{m}}$ lies in the (001) plane and is perpendicular to $\boldsymbol{m}$, so that $\boldsymbol{I}_{\mathrm{s}} \perp \boldsymbol{n}$. In configuration 2, the rotation plane is changed to (100), $\dot{\boldsymbol{m}}$ lies along the [100] direction, and $\boldsymbol{I}_{\mathrm{s}}$ lies in the (100) plane. The relation $\boldsymbol{I}_{\mathrm{s}} \perp \boldsymbol{n}$ still holds. No appreciable angular dependence is observed for either rotation plane. The system displays an isotropic damping, consistent with the magnetic isotropy inferred from the band-structure calculations.

In the decoupled regime, where the interlayer coupling is weak, the ferromagnetic and antiferromagnetic moments evolve independently. We first examine the limiting case in which the pumped spin-current polarization is always parallel to the Néel vector. We realize this case in two ways. In configuration 4, $\boldsymbol{n} \parallel [001]$ is fixed, $\boldsymbol{m}$ rotates within the (001) plane, $\dot{\boldsymbol{m}}$ lies in the (001) plane and perpendicular to $\boldsymbol{m}$, and $\boldsymbol{I}_{\mathrm{s}}$ points along the [001] direction, which is parallel to $\boldsymbol{n}$ ($\boldsymbol{I}_{\mathrm{s}} \parallel \boldsymbol{n}$). In configuration 5, $\boldsymbol{m}$ and $\boldsymbol{n}$ co-rotate within the (001) plane while keeping $\boldsymbol{m} \perp \boldsymbol{n}$. The perturbation $\dot{\boldsymbol{m}}$ is applied along the [001] direction, and $\boldsymbol{I}_{\mathrm{s}}$ is perpendicular to $\boldsymbol{m}$ and parallel to $\boldsymbol{n}$ ($\boldsymbol{I}_{\mathrm{s}} \parallel \boldsymbol{n}$). In both configurations, φ is swept from 0° to 180°. The damping enhancement indicated by the red and blue symbols in Fig. 3(b) is close to zero in both cases, which demonstrates that spin-current absorption by the AFM is strongly suppressed when the spin-current polarization is parallel to the Néel vector.

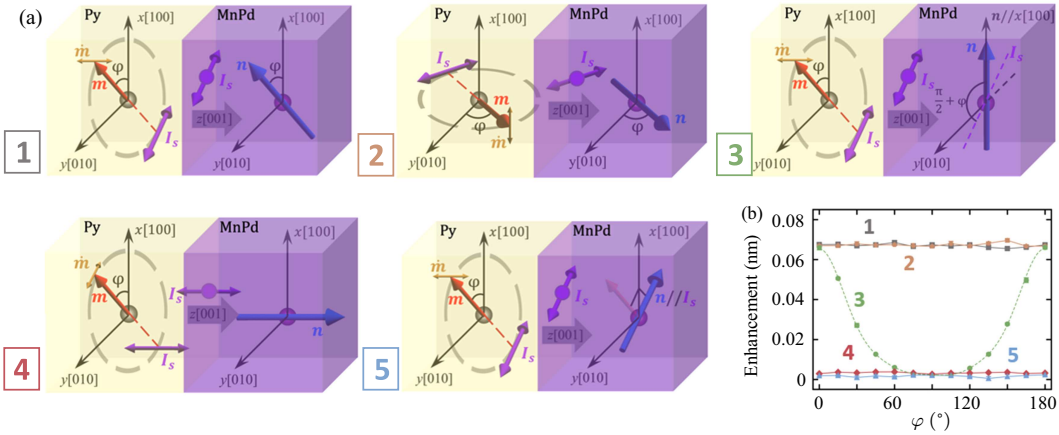


Fig. 3. (a) Schematic illustrations of the Néel order, magnetic moment, moment perturbation, and spin-current directions for configurations 1–5. (b) Damping enhancement as a function of the FM magnetization angle φ for configurations 1–5, together with a cosine-series fit for configuration 3 (green dashed line). The color code is gray for configuration 1, orange for configuration 2, green for configuration 3, red for configuration 4, and blue for configuration 5.

Next, we consider a configuration that continuously interpolates between the two limiting cases. In configuration 3 [green curve in Fig. 3(b)], $\boldsymbol{n} \parallel [100]$ is fixed, $\boldsymbol{m}$ rotates within the (001) plane with φ measured from [100], $\dot{\boldsymbol{m}}$ lies along the [001] direction, and $\boldsymbol{I}_{\mathrm{s}}$ lies in the (001) plane perpendicular to $\boldsymbol{m}$. The angle between $\boldsymbol{I}_{\mathrm{s}}$ and $\boldsymbol{n}$ is therefore $\pi/2 + \varphi$. The damping enhancement reaches its maximum at $\varphi = 0°$ and 180°, coinciding with configurations 1 and 2, and its minimum at $\varphi = 90°$, coinciding with configurations 4 and 5. The angular dependence shows a pronounced twofold symmetry with a weaker fourfold component. Fitting the data with

$$D = D_0 + D_2 \cos 2(\varphi + \varphi_2) + D_4 \cos 4(\varphi + \varphi_4) + D_6 \cos 6(\varphi + \varphi_6) + D_8 \cos 8(\varphi + \varphi_8) \quad (1)$$

yields $D_2 = (2.81 \pm 0.02) \times 10^{-2}$, $D_4 = (1.06 \pm 0.02) \times 10^{-2}$, $D_6 = (3.5 \pm 0.2) \times 10^{-3}$, and $D_8 = (1.0 \pm 0.2) \times 10^{-3}$, with all values given in units of nanometers. Among these terms, D_2 and D_4 have well-defined physical origins: the dominant twofold component D_2 arises from the vector structure of the spin-transfer torque [Eqs. (2) and (3)] and confirms the $\cos^2\varphi$ dependence, while D_4 is attributed to the fourfold in-plane crystalline anisotropy of $L1_0$-MnPd along the transport direction. A pronounced fourfold damping anisotropy has also been observed experimentally in epitaxial manganite thin films, where it was discussed in terms of crystalline symmetry, orientation-dependent spin–orbit coupling, orbital degrees of freedom, and defect-related scattering.[37] This supports the assignment of the D_4 component to symmetry-allowed anisotropic spin relaxation rather than to a purely numerical fitting artifact. The weaker D_6 and D_8 terms are retained as higher-order Fourier components of the complete heterostructure response. We truncate the expansion at D_8 because including still higher harmonics (D_{10} and above) leaves D_2 and D_4 unchanged within their error bars, indicating that the cosine-series expansion has converged.

The observed twofold angular dependence can be derived directly from the spin-pumping picture.[30,38] For a small-angle precession, the pumped spin current satisfies $\boldsymbol{I}_s^{\mathrm{pump}} \propto \boldsymbol{m} \times \dot{\boldsymbol{m}}$, so its polarization is always perpendicular to the instantaneous FM magnetization and follows the tangent of the precession trajectory. In configuration 3, the Néel vector is fixed along [100] while the FM magnetization rotates in the (001) plane, so the angle between the spin-current polarization and the Néel vector is $\pi/2 + \varphi$. The spin-transfer torque acting on the AFM is then

$$\begin{aligned} &\boldsymbol{\tau}_{\mathrm{STT}} \propto \boldsymbol{n} \times (\boldsymbol{I}_s \times \boldsymbol{n}) \\ &= 2[\boldsymbol{m}_1 \times (\boldsymbol{I}_s \times \boldsymbol{m}_1) + \boldsymbol{m}_2 \times (\boldsymbol{I}_s \times \boldsymbol{m}_2)] \\ &\propto |\boldsymbol{I}_s| \sin\left(\frac{\pi}{2} + \varphi\right), \end{aligned} \tag{2}$$

where $\boldsymbol{m}_1$, $\boldsymbol{m}_2$, and $\boldsymbol{n}$ are defined as before. The spin-transfer torque enters the LLG equation as an additional contribution to the magnetization rate of change, $\dot{\boldsymbol{m}}|_{\mathrm{STT}} \propto \boldsymbol{\tau}_{\mathrm{STT}}$,[25] while the energy dissipation rate associated with magnetization dynamics is quadratic in $\dot{\boldsymbol{m}}$, $\dot{E} = (\mu_0 M_s V \alpha/\gamma)|\dot{\boldsymbol{m}}|^2$, as follows directly from the Gilbert form of the LLG equation.[11,12] The associated dissipation therefore scales as

$$\dot{E}_{\mathrm{STT}} \propto |\boldsymbol{\tau}_{\mathrm{STT}}|^2 \propto I_s^2 \sin^2\left(\frac{\pi}{2} + \varphi\right) = I_s^2 \cos^2\varphi, \tag{3}$$

which reproduces the dominant twofold component observed in configuration 3. The damping is governed by the vector structure of the spin-transfer torque, so spin-current absorption is maximal when the pumped spin-current polarization is perpendicular to the Néel vector and minimal when it is parallel. Accordingly, the damping enhancement at $\varphi = 0^\circ$ and 180° coincides with that of configurations 1 and 2, whereas the minimum at $\varphi = 90^\circ$ agrees with the results of configurations 4 and 5. The five configurations are mutually consistent and demonstrate that the damping enhancement is controlled mainly by the dissipation of the spin current pumped from the FM into the AFM rather than by the absolute orientation of the Néel order itself.

In summary, these results establish a perpendicular absorption and parallel reflection picture. When the spin-current polarization is perpendicular to the Néel vector, the AFM serves as an efficient spin sink that rapidly dissipates spin angular momentum, resulting in a pronounced damping enhancement. When the spin-current polarization is parallel to the Néel vector, spin accumulation builds up on the side of the interface adjacent to the AFM and generates a strong backflow spin current. This backflow suppresses the net spin-current injection and markedly reduces the damping enhancement.

The applicability of this picture beyond the present collinear metallic MnPd system should be considered with care. For more complex systems based on AFMs, the detailed angular dependence is not expected to coincide with that of $L1_0$-MnPd. (i) In noncollinear metallic AFMs such as $IrMn_3$ or Mn_3Sn, the total damping response requires a vector summation of the STTs over all magnetic sublattices, so the resulting symmetry depends jointly on the magnetic structure, the film orientation, uncompensated moments, and interfacial disorder, as illustrated by the fourfold damping anisotropy reported in $CoFeB/IrMn_3$ bilayers.[24] (ii) In polycrystalline AFMs such as FeMn or IrMn, the measured anisotropy further averages over grain orientations and domain distributions, which accounts for both the smooth angular dependence in NiFe/Cu/FeMn spin valves[26] and the abrupt changes within fixed angular intervals in exchange-spring Pt/FeMn/FeNi films.[25] (iii) In insulating AFMs such as CoO or NiO, itinerant electrons cannot traverse the AFM, so the scattering-matrix STT mechanism considered here is no longer applicable and the damping must instead be analyzed in terms of the interfacial spin-mixing conductance and magnon-mediated spin transport, consistent with the Néel-orientation-insensitive Fe damping observed in Py/CoO/Ag/Fe heterostructures.[27] In addition, strong interfacial spin–orbit coupling can introduce Rashba-type torques and spin-memory loss that superpose on the STT-driven response. More broadly, spin-transfer torque and chiral interactions such as the Dzyaloshinskii–Moriya interaction have also been shown to engineer nonreciprocal spin-wave damping and polarization in ferromagnetic systems,[44] illustrating the wider relevance of torque-controlled damping in magnonic devices. These factors may modify the Fourier coefficients, shift their phases, or introduce extra angular components, but they do not affect the central conclusion of the present MnPd/Py study, namely that

the dominant damping modulation originates from the relative orientation between the pumped spin-current polarization and the Néel vector.

We then turn to the experimental relevance of these configurations. Configurations 1 and 2 can be regarded as idealized strong-coupling limits of exchange-biased or exchange-spring FM/AFM bilayers, where interfacial or rotatable antiferromagnetic moments can be partially dragged by the FM magnetization.[25,39,40] Configuration 3, in which $\boldsymbol{m}$ rotates freely while $\boldsymbol{n}$ is pinned along an easy axis by a strong uniaxial anisotropy or by a field-cooling procedure, is closer to epitaxial $L1_0$-MnPd or MnPt heterostructures with a well-defined uniaxial anisotropy, and is consistent with the angular dependence reported by Polishchuk *et al*. in NiFe/Cu/FeMn spin valves.[26] Configurations 4 and 5 are idealized limits designed to isolate the case in which the pumped spin-current polarization is parallel to $\boldsymbol{n}$. They are difficult to realize directly in experiments but serve as useful theoretical references.

Having clarified the experimental relevance of the five magnetic configurations, we finally comment on the use of the symmetric heterostructure in our calculations. If the symmetric Cu|MnPd|Py|MnPd|Cu geometry is relaxed to an asymmetric Cu|MnPd|Py|Cu stack, one of the two MnPd|Py interfaces is replaced by a Cu|Py interface. Because the angular dependence established above is a local property of a single MnPd|Py interface, removing one such interface is expected to preserve the $\cos^2\varphi$ dominance and the relative weight of D_4, while the absolute magnitudes of D_2 and D_4 are roughly halved. The additional Cu|Py interface contributes mainly a φ-independent term to D_0. This expectation is consistent with the experiment of Polishchuk *et al*.[26] on NiFe/Cu/FeMn spin valves, an asymmetric stack that nevertheless exhibits the same $\cos^2\varphi$-type angular dependence with the damping maximized for spin-current polarization perpendicular to the Néel vector. The key conclusions of this work are therefore expected to remain qualitatively unchanged in asymmetric Cu|MnPd|Py|Cu heterostructures.

3.3. Further tests

To test whether the above conclusions remain valid in realistic systems, we introduce two categories of perturbation: thermal disorder and interface disorder. Thermal disorder is further divided into spin disorder and lattice disorder. To focus on how the Néel order affects spin-current absorption and to enable a direct comparison with the ideal case, the spin disorder is applied only to the MnPd layer in configuration 3 [green curve in Fig. 3(b)]. As shown in Fig. 4(a), the results are obtained for $\varphi = 45^\circ$ (filled circles) and $\varphi = 90^\circ$ (open circles). In both cases, stronger spin disorder, reflected by a smaller $\langle M\rangle/M_s$, leads to a modest increase in the damping enhancement. The omission of ferromagnetic spin fluctuations in Fig. 4(a) is justified on two grounds: (i) ferromagnetic spin fluctuations would contribute mainly to the slope of the linear fit in Fig. 2(c), i.e., to the intrinsic damping α_0, rather than to the intercept that is the focus of our analysis.[9,36] Moreover, Starikov *et al*. showed that spin disorder produces only a weak change in the damping parameter of $Ni_{80}Fe_{20}$ even for sizable rms rotations of the local magnetic moments;[36] and (ii) the pumped spin current $\boldsymbol{I}_s^{\rm pump} \propto \boldsymbol{m}\times\dot{\boldsymbol{m}}$ follows the macroscopic Py magnetization, so small ferromagnetic fluctuations only rescale $|\boldsymbol{I}_s|$ without altering its direction, while the angular dependence — set by the relative orientation of $\boldsymbol{I}_s$ and $\boldsymbol{n}$ through Eqs. (2) and (3) — is insensitive to such fluctuations. Ferromagnetic spin fluctuations therefore do not affect our conclusion of Néel-order-controlled damping anisotropy.

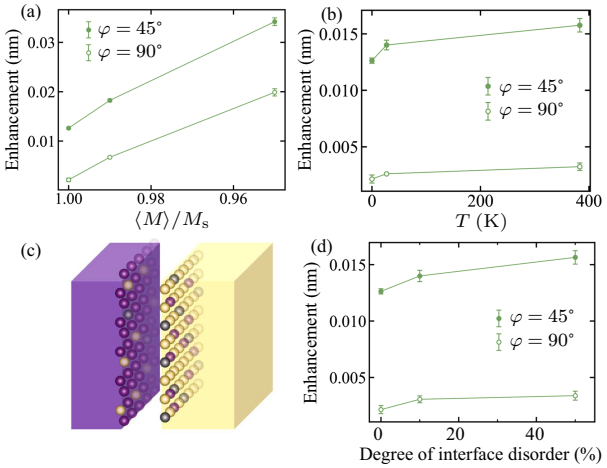


Fig. 4. (a) Damping enhancement as a function of $\langle M\rangle/M_s$ at $\varphi = 45^\circ$ (filled circles) and $\varphi = 90^\circ$ (open circles). (b) Damping enhancement as a function of temperature (lattice disorder) at $\varphi = 45^\circ$ (filled circles) and $\varphi = 90^\circ$ (open circles). (c) Schematic of the MnPd|Py interface disorder. (d) Damping enhancement as a function of the interface disorder degree at $\varphi = 45^\circ$ (filled circles) and $\varphi = 90^\circ$ (open circles).

For the lattice disorder, which is likewise applied only to the MnPd layer, the disorder strength is characterized by the root-mean-square atomic displacement Δ. The two disorder strengths $\Delta/a = 0.024$ and 0.048 are related to temperature through the Debye temperature $\Theta_D = 377$ K of MnPd[41] via

$$\Delta^2 = \frac{9\hbar^2}{Mk_B\Theta_D}\left(\frac{T^2}{\Theta_D^2}\int_0^{\Theta_D/T}\frac{x}{e^x-1}\,dx+\frac{1}{4}\right), \tag{4}$$

which gives $\Delta/a = 0.024$ and 0.048, corresponding to temperatures of 27 K and 383 K, respectively. As shown in Fig. 4(b), lattice disorder has no appreciable effect on the spin-pumping-dominated damping enhancement. Although finite temperature enhances scattering in the system, its contribution to spin-current dissipation is limited. Its effect is much weaker than the spin-transfer-torque modulation induced by changes in the magnetic-moment orientation, and is also smaller than that of spin disorder.

Finally, we introduce interface disorder to simulate atomic intermixing at realistic interfaces. As shown in

Fig. 4(c), a specified number of interface atoms are randomly selected and swapped with atoms at random positions in the adjacent layer. The same procedure is applied symmetrically to both MnPd|Py interfaces of the Cu|MnPd|Py|MnPd|Cu heterostructure, so that both interfaces share the same disorder concentration. For each disorder concentration, five independent random samples are generated, and the reported damping enhancement is the average over these five samples. The corresponding error bars represent the standard deviation among them. Figure 4(d) presents results for $\varphi = 45^\circ$ (filled circles) and $\varphi = 90^\circ$ (open circles). As the disorder increases, that is, as a larger fraction of Mn atoms are exchanged with atoms in the Py layer, both sets of damping enhancement rise modestly. This behavior arises because atomic interdiffusion disrupts the ideal translational symmetry of the interface and enhances spin-dependent scattering. This picture is also consistent with first-principles studies showing that lattice mismatch and interface alloying strongly enhance interfacial spin-memory loss,[42,43] thereby modifying the spin-current transmission across the interface. Nevertheless, even in the extreme case of 50% atomic exchange, the change in damping enhancement remains limited. This indicates that Néel-order-dependent angular-momentum dissipation still dominates the damping enhancement of the system.

We next examine how the damping enhancement depends on the MnPd layer thickness. As shown in Fig. 5, we take $\varphi = 45^\circ$ as a representative case. Configurations 1 (gray squares) and 3 (green circles) are both calculated for 11, 5, and 2 atomic layers of MnPd. Both sets are extended to the limiting case of a single Mn monolayer, indicated by dashed lines. For configuration 1, the damping enhancement remains relatively stable from 5 to 11 layers and increases only slightly when the system is thinned to a single Mn monolayer. For configuration 3, the damping enhancement increases significantly as the MnPd thickness decreases and reaches a maximum in the single-Mn-monolayer limit.

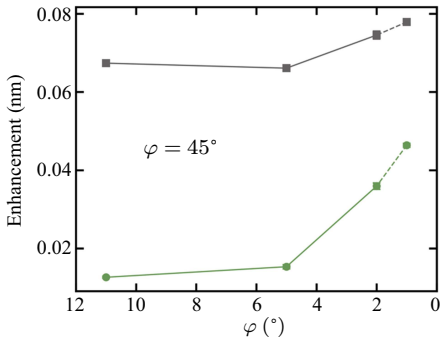


Fig. 5. Damping enhancement at $\varphi = 45^\circ$ for configuration 1 (gray squares) and configuration 3 (green circles) as a function of the number of MnPd atomic layers. Solid lines connect the results for 2 to 11 atomic layers. Dashed lines extend to the limiting case of a single Mn monolayer.

The contrasting thickness dependences originate from the different responses of the Mn layers to the spin current in the two configurations. In this heterostructure, the spin current pumped from Py dissipates through two channels, namely absorption by the Mn sublattice within MnPd and transmission through MnPd into the semi-infinite Cu electrode, which acts as a perfect spin sink. The Pd layers provide no dissipation channel and mainly reflect the incident spin current back toward the FM, where the reflected part no longer contributes to the damping enhancement. In configuration 1, the short spin-diffusion length in MnPd[18] concentrates the Mn absorption within the first few layers next to the Mn|Py interface, so five layers of MnPd already absorb essentially all the spin current entering MnPd. Additional layers beyond this thickness merely act as redundant Pd reflectors or lie outside the active spin-diffusion region, and the damping enhancement therefore saturates between 5 and 11 layers. When MnPd is further thinned to 2 layers or the single-Mn-monolayer limit, the reduced number of Pd reflectors allows part of the spin current to traverse MnPd and reach the opposite Cu electrode, converting the reflection-back-to-FM channel into an escape-into-Cu dissipation channel and slightly enhancing the damping. In configuration 3, the angle between the spin-current polarization and the Néel vector changes from 90° to 135° relative to configuration 1, making the Mn layers more reflective to the spin current and weakening the effective spin absorption. When the MnPd layer is thinned, the reduction in the number of Pd layers, together with the enhanced Mn reflectivity, strongly shortens the multiple-reflection path of the spin current within the AFM. This substantially increases the net spin current, so the damping enhancement grows much more strongly than in configuration 1. The same Pd-reflection/Cu-electrode-dissipation picture accounts for this stronger thickness dependence: the higher Mn reflectivity makes the reflection-back-to-FM channel more dominant in configuration 3, so removing Pd reflectors releases a larger fraction of the spin current into the Cu electrode. In the single-Mn-monolayer limit, the Pd reflector layers are completely absent, and the spin current is no longer reflected back into the AFM interior. Instead, it enters the Cu electrode directly and dissipates at infinity, yielding the maximum damping enhancement. The thickness dependences of both configurations therefore confirm that the damping enhancement originates from the additional angular-momentum dissipation induced by spin pumping.

We then test whether the angular dependence survives when the AFM and FM are separated by a Cu spacer. For configuration 3, we insert a 2-layer Cu spacer between the AFM and FM and compute the full angular dependence from $\varphi = 0^\circ$ to 180°. The results are shown as black data points in Fig. 6(a). For comparison, the result of configuration 3 without a Cu spacer is replotted. After Cu insertion, the system still exhibits a pronounced angular dependence, and the overall behavior remains qualitatively consistent with the original

configuration 3. This agrees with the experimental observation by Polishchuk *et al*. in a NiFe/Cu/FeMn spin valve, where the angular dependence of the damping survives through the Cu spacer.[26] That experiment also found that the damping enhancement is maximized when the spin-current polarization is perpendicular to the Néel vector.

Our first-principles calculations reveal the microscopic origin of this behavior. The vector structure of the spin-transfer torque dictates that the AFM can efficiently dissipate angular momentum only when the pumped spin current is perpendicular to the Néel vector. Fitting with Eq. (1) (dashed line in the figure) yields $D_2 = (1.74 \pm 0.01) \times 10^{-2}$, $D_4 = (5.2 \pm 0.1) \times 10^{-3}$, $D_6 = (1.6 \pm 0.1) \times 10^{-3}$, and $D_8 = (0.4 \pm 0.1) \times 10^{-3}$, with all values given in units of nanometers. These values are consistent with the earlier configuration 3 results: the twofold component remains dominant, and the higher-order terms are small. Notably, the damping enhancement at $\varphi = 0^\circ$ decreases significantly relative to other angles. This is because inserting the Cu spacer replaces the original MnPd|Py interface with a Cu|Py interface, which alters the interface structure and modifies the spin-flip probability. Even so, efficient spin-transport channels remain in the Cu layer, allowing the spin current to traverse the spacer and reach the MnPd spin sink. The damping-enhancement intercept after Cu insertion is $(4.18 \pm 0.04) \times 10^{-2}$ (nm), close to the value $(4.89 \pm 0.02) \times 10^{-2}$ (nm) calculated for the Cu|Py|Cu system [Fig. 2(c)]. This confirms that the observed change originates from the modified interface structure.

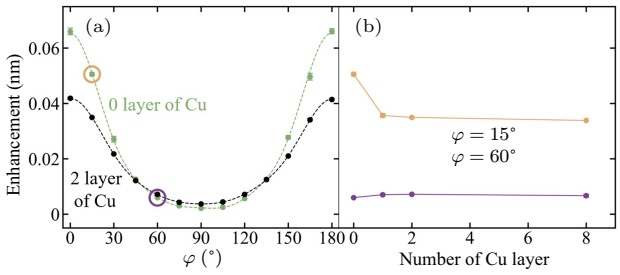


Fig. 6. (a) Angular dependence of the damping enhancement for configuration 3 with a 2-layer Cu spacer inserted (black circles with dashed-line fit), compared with the configuration 3 result without a Cu spacer (green circles with dashed-line fit). Yellow and purple circles mark the data points at $\varphi = 15^\circ$ and $\varphi = 60^\circ$, respectively. (b) Damping enhancement as a function of the number of Cu spacer layers at $\varphi = 15^\circ$ (yellow) and $\varphi = 60^\circ$ (purple).

To test the thickness effect of the Cu spacer layer, we then choose $\varphi = 15^\circ$ and $\varphi = 60^\circ$ as two representative angles, marked by yellow and purple circles in Fig. 6(a). For these two angles, we compute the damping enhancement after inserting 1, 2, and 8 Cu spacer layers, as shown in Fig. 6(b). At $\varphi = 15^\circ$ (yellow), the damping enhancement decreases with increasing Cu thickness and then saturates. Cu is a weak spin absorber, whereas MnPd is an efficient spin-dissipation layer. As a result, the spin current accumulates in the Cu layer and generates a spin backflow. With increasing Cu thickness, both the spin accumulation and the backflow current grow, which reduces the net spin current reaching the MnPd layer and thus lowers the damping enhancement.[3] At $\varphi = 60^\circ$ (purple), the damping enhancement is nearly insensitive to the Cu thickness. In this case, the spin-current polarization is nearly parallel to the Néel vector, so MnPd absorption is strongly suppressed and reflection dominates. Although the additional interfaces introduced by the Cu spacer can generate extra interfacial spin-flip scattering and spin-memory loss,[42,43] thereby modifying the effective spin transmission across the spacer stack, the damping enhancement itself is small. The corresponding effect is therefore negligible.

4. Conclusion

In this work, we combined spin-pumping theory with the first-principles scattering-matrix method to investigate how the $L1_0$-MnPd AFM layer modulates the damping of an adjacent Py layer in the symmetric heterostructure Cu|MnPd|Py|MnPd|Cu. Our results demonstrate that the damping enhancement depends sensitively on the angle between the pumped spin-current polarization and the Néel vector. When the spin-current polarization is perpendicular to the Néel vector, the AFM absorbs angular momentum efficiently and the FM damping is substantially enhanced. When the polarization is parallel to the Néel vector, spin accumulation and backflow suppress the net spin-current injection, markedly reducing the damping enhancement. Quantitatively, the angular dependence exhibits a dominant twofold symmetry (D_2), which can be attributed to the vector structure of the spin-transfer torque, and a weaker fourfold component (D_4), which arises from the fourfold crystalline anisotropy of MnPd along the transport direction. Additional tests involving Cu-spacer insertion, MnPd thickness variation, and several forms of disorder — including spin, lattice, and interface disorder — confirm the robustness of this mechanism. These results identify the Néel order as a new degree of freedom for tuning FM damping and provide a theoretical foundation for designing AFM-based spintronic devices with controllable damping. We emphasize that the present conclusions are obtained for the specific case of a metallic and collinear AFM, $L1_0$-MnPd, treated within the first-principles scattering-matrix framework combined with spin-pumping theory. Their extension to non-collinear or insulating AFMs, or to systems with strong interfacial spin–orbit coupling, may require additional considerations and is left for future study.

Appendix A: Discussion of Pd magnetic moments in MnPd

Whether Pd atoms carry a magnetic moment in $L1_0$-MnPd has been discussed in the literature. Krén and

Sólyom[28] studied the antiferromagnetic structure of MnPd by neutron diffraction and obtained a Mn sublattice moment of $\mu_{\mathrm{Mn}} = 4.4 \pm 0.4\ \mu_{\mathrm{B}}$ and a Néel temperature of $T_{\mathrm{N}} = 813 \pm 10$ K. They further noted that the exchange interaction at the Pd site vanishes, so any Pd moment can arise only from much weaker anisotropic interactions. The Pd moment should therefore be negligibly small, and they adopted $\mu_{\mathrm{Pd}} \approx 0$ in their diffraction analysis. Yamada *et al*. performed GGA-LMTO-ASA first-principles band-structure and total-energy calculations for CuAu-I-type MnPd.[33] Among the candidate magnetic orderings, including FM and three AFM arrangements, the lowest total energy corresponds to a configuration with a Mn moment of 3.28 μ_{B}, antiferromagnetic alignment between Mn atoms, and a vanishing Pd moment. The resulting equilibrium lattice constants, $a^* = a/\sqrt{2} \approx 2.89$ Å and $c \approx 3.60$ Å, agree well with the values $a^* \approx 2.88$ Å and $c \approx 3.58$ Å adopted here. In contrast, the FM state can induce a Pd moment of about 0.31 μ_{B}, but its total energy is higher than that of the ground state by 12.5 mRy/f.u. and is therefore not competitive.[33]

To further assess the effect of the Pd magnetic moment on the stability of MnPd, we compute the electronic structure and total energy for two magnetic structures in which the Pd atoms carry finite moments (denoted structures B and C). We compare them with the ground-state magnetic structure discussed in the main text, in which the Pd moment vanishes. As shown in Fig. A1, the band dispersions of structures B and C differ markedly from those of the ground-state configuration in Fig. 1. Band crossings and near-degeneracies near the Fermi level undergo pronounced splitting and rearrangement. The overall number and distribution of bands also change. This reflects the fact that different magnetic structures correspond to different magnetic translation symmetries, which modify the magnetic unit cell, band folding, and the allowed hybridization channels.

Total-energy calculations show that, taking the ground-state configuration (Néel order along x) as the reference, structures B and C are higher in energy by approximately 10^1 eV. This is far larger than the 10^{-2} eV-scale energy differences caused by rotating the Néel-vector direction within the same magnetic structure. Meanwhile, the density-of-states calculations reveal a significantly increased spectral weight near the Fermi level in structures B and C. This pronounced change is consistent with a much less stable electronic configuration and with the substantially higher total energies of these two states. Krén and Sólyom[28] concluded from neutron diffraction that the exchange interaction at the Pd site vanishes and therefore assumed $\mu_{\mathrm{Pd}} \approx 0$. Yamada *et al*.[33] reached the same conclusion from first-principles calculations. Our total-energy calculations further support this picture: finite-Pd-moment configurations are higher in energy by approximately 10^1 eV, confirming that such configurations do not represent the ground-state magnetic structure of $L1_0$-MnPd.

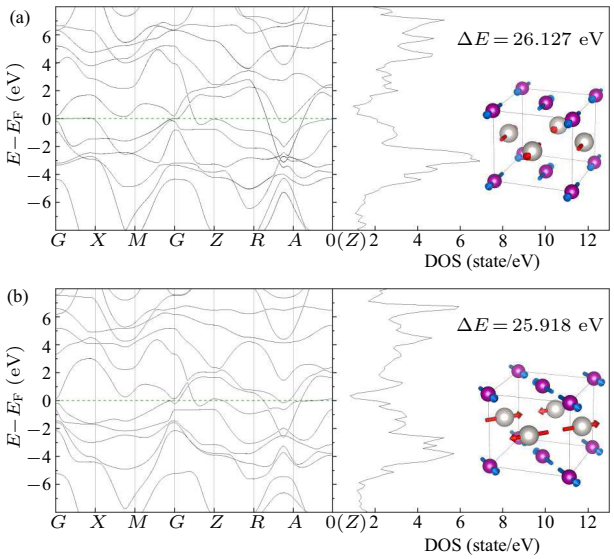


Fig. A1. Band dispersion and density of states for magnetic structures B (a) and C (b), in which the Pd atoms carry finite magnetic moments. Compared with the ground-state structure [Figs. 1(a)–1(c)], the band topology near the Fermi level is significantly altered.

Acknowledgements

We gratefully acknowledge HZWTECH for providing computing facilities. This work was supported by the National Key Research and Development Program of China (Grant No. 2024YFA1408500) and the National Natural Science Foundation of China (Grant Nos. 12374101 and 12574115).

References

[1] Mizukami S, Ando Y and Miyazaki T 2001 *Jpn. J. Appl. Phys.* **40** 580
[2] Urban R, Woltersdorf G and Heinrich B 2001 *Phys. Rev. Lett.* **87** 217204
[3] Mizukami S, Ando Y and Miyazaki T 2002 *Phys. Rev. B* **66** 104413
[4] Bhagat S M and Lubitz P 1974 *Phys. Rev. B* **10** 179
[5] Xu Z, Zhang K and Li J 2021 *Phys. Rev. B* **104** 224404
[6] Beaujour J M L, Lee J H, Kent A D, Krycka K and Kao C C 2006 *Phys. Rev. B* **74** 214405
[7] Walowski J, Djordjevic Kaufmann M, Lenk B, Hamann C, McCord J and Münzenberg M 2008 *J. Phys. D: Appl. Phys.* **41** 164016
[8] Gilmore K, Idzerda Y U and Stiles M D 2007 *Phys. Rev. Lett.* **99** 027204
[9] Liu Y, Starikov A A, Yuan Z and Kelly P J 2011 *Phys. Rev. B* **84** 014412
[10] Tserkovnyak Y, Brataas A and Bauer G E W 2002 *Phys. Rev. Lett.* **88** 117601
[11] Tserkovnyak Y, Brataas A, Bauer G E W and Halperin B I 2005 *Rev. Mod. Phys.* **77** 1375
[12] Brataas A, Tserkovnyak Y and Bauer G E W 2008 *Phys. Rev. Lett.* **101** 037207
[13] Huang Z, Tang X, Chen Q, Jiang W, Guo Q, Jalali M, Du J and Zhai Y 2024 *Chin. Phys. B* **33** 097202
[14] Saitoh E, Ueda M, Miyajima H and Tatara G 2006 *Appl. Phys. Lett.* **88** 182509
[15] Hahn C, de Loubens G, Viret M, Klein O, Naletov V V and Ben Youssef J 2013 *Phys. Rev. Lett.* **111** 217204
[16] Jungwirth T, Martí X, Wadley P and Wunderlich J 2016 *Nat. Nanotechnol.* **11** 231
[17] Baltz V, Manchon A, Tsoi M, Moriyama T, Ono T and Tserkovnyak Y 2018 *Rev. Mod. Phys.* **90** 015005
[18] Zhang W, Jungfleisch M B, Jiang W, Pearson J E, Hoffmann A, Freimuth F and Mokrousov Y 2014 *Phys. Rev. Lett.* **113** 196602

[19] Qiu Z, Li J, Hou D, Arenholz E, N'Diaye A T, Tan A, ichi Uchida K, Sato K, Okamoto S, Tserkovnyak Y, Qiu Z Q and Saitoh E 2016 *Nat. Commun.* **7** 12670

[20] Wang Y, Decker M M, Meier T N G, Chen X, Song C, Grünbaum T, Zhao W, Zhang J, Chen L and Back C H 2020 *Nat. Commun.* **11** 275

[21] Meiklejohn W H and Bean C P 1957 *Phys. Rev.* **105** 904

[22] Frangou L, Oyarzún S, Auffret S, Vila L, Gambarelli S and Baltz V 2016 *Phys. Rev. Lett.* **116** 077203

[23] Saglam H, Zhang W, Jungfleisch M B, Sklenar J, Pearson J E, Ketterson J B and Hoffmann A 2016 *Phys. Rev. B* **94** 140412

[24] Wang Y, Feng X, Yan Z, Xue K, Zhu X and Zhan Q 2024 *Appl. Phys. Lett.* **124** 012404

[25] Moriyama T, Kamiya M, Oda K, Tanaka K, Kim K J and Ono T 2017 *Phys. Rev. Lett.* **119** 267204

[26] Polishchuk D M, Kamra A, Polek T I, Brataas A and Korenivski V 2019 *Phys. Rev. Lett.* **123** 247201

[27] Yang M, Li Q, Hou D, Shafer P, N'Diaye A T, Klewe C, Wang T Y, Zhang X, Hwang C and Qiu Z Q 2020 *Phys. Rev. B* **101** 224418

[28] Krén E and Sólyom J 1966 *Phys. Lett.* **22** 273

[29] Gu J W and Zhou S M 2023 *Phys. Rev. B* **108** 054420

[30] Liu Y, Yuan Z, Wesselink R J H, Starikov A A and Kelly P J 2014 *Phys. Rev. Lett.* **113** 207202

[31] Xia K, Zwierzycki M, Talanana M, Kelly P J and Bauer G E W 2006 *Phys. Rev. B* **73** 064420

[32] Blöchl P E 1994 *Phys. Rev. B* **50** 17953

[33] Yamada H, Shimizu H, Yamamoto K and Uebayashi K 2006 *J. Alloys Compd.* **415** 31

[34] Andersen O K, Pawlowska Z and Jepsen O 1986 *Phys. Rev. B* **34** 5253

[35] Starikov A A, Kelly P J, Brataas A, Tserkovnyak Y and Bauer G E W 2010 *Phys. Rev. Lett.* **105** 236601

[36] Starikov A A, Liu Y, Yuan Z and Kelly P J 2018 *Phys. Rev. B* **97** 214415

[37] Ren J, Zhang Y, Cai M, Li Y, Li M, Wang T, Shen D, Zhou H, Zhu X and Zhang J 2025 *Chin. Phys. B* **34** 107504

[38] Cheng R, Xiao J, Niu Q and Brataas A 2014 *Phys. Rev. Lett.* **113** 057601

[39] Martí X, Park B G, Wunderlich J, Reichlová H, Kurosaki Y, Yamada M, Yamamoto H, Nishide A, Hayakawa J, Takahashi H and Jungwirth T 2012 *Phys. Rev. Lett.* **108** 017201

[40] Wang W, Chai G and Xue D 2017 *Sci. Rep.* **7** 1341

[41] Wang J, Gao A, Chen W, Zhang X D, Zhou B and Jiang Z 2013 *J. Magn. Magn. Mater.* **333** 93

[42] Gupta K, Wesselink R J H, Liu R, Yuan Z and Kelly P J 2020 *Phys. Rev. Lett.* **124** 087702

[43] Liu R, Gupta K, Yuan Z and Kelly P J 2022 *Phys. Rev. B* **106** 014401

[44] Liu X, Wang X, Li Z, Han X and Guo G 2026 *Chin. Phys. B* **35** 047502